Science Advances
AAAS

Supplementary Materials for

The effect of renewable energy incorporation on power grid stability and resilience

Oliver Smith*, Oliver Cattell, Etienne Farcot, Reuben D. O'Dea, Keith I. Hopcraft

*Corresponding author. Email: oliver.smith@nottingham.ac.uk

Published 2 March 2022, *Sci. Adv.* **8**, eabj6734 (2022)
DOI: 10.1126/sciadv.abj6734

This PDF file includes:

Power grid model

Swing equation derivation

We model power networks using the swing equation: a second order oscillator model that captures transient dynamics. Each node on the network may be a generator or consumer, with positive or negative net power output respectively. The swing equation is long established in the electrical engineering literature as an accurate model of power grid dynamics. Full derivations of the model, together with stability analyses are available (*28, 29*). This section summarises the swing equation's derivation and defines the various parameters used in the main paper. Further details on the stability analysis of the elementary two-node case are also included.

To begin the derivation, we note that each node i in the network is modelled as a rotating machine with phase angle

$$\phi_i(t) = \Omega t + \theta_i(t), \tag{S1}$$

where Ω is the grid's reference frequency, typically $2\pi \times 50\,\mathrm{Hz}$ or $2\pi \times 60\,\mathrm{Hz}$, and θ is the machine's phase difference. Classically, these nodes are either conventional generators with spinning inertia, or power consumers (often referred to as loads). These loads may be modelled as constant impedances, but it is also common to model the consumers/loads as a type of rotating machine themselves (*15*) with negative power demand. This is the approach adopted in this work since it preserves the structure of the underlying network. Generators may also be direct-current sources such as photovoltaic (PV) panels. These generator's control systems can emulate the inertial properties of conventional generator (*42*), allowing the use of the swing equation.

Power must be conserved at each node a power grid; thus, the dissipative P_i^{diss} and inertial P_i^{iner} power must balance the machine's mechanical power P_i^{mech} and the power P_i^{elec} being transmitted to and from the rest of the network. The inertial and dissipative terms are given by

$$P_i^{\text{iner}} = \frac{1}{2} J_i \frac{\mathrm{d}}{\mathrm{d}t} \left(\frac{\mathrm{d}\phi_i}{\mathrm{d}t} \right)^2 \tag{S2}$$

and

$$P_i^{\text{diss}} = D_i \left(\frac{\mathrm{d}\phi_i}{\mathrm{d}t} \right)^2, \tag{S3}$$

where J_i is the moment of inertia and D_i is a damping coefficient. Assuming the impedances of the grid's connections are largely reactive, and that the voltage across the network is approximately constant at V_0, then the transmitted electrical power is given by

$$P_i^{\text{elec}} = \sum_{j=1}^{n} V_0^2 B_{ij} \sin(\theta_i - \theta_j), \tag{S4}$$

where B_{ij} is the electrical susceptance of edge ij. Substituting Eq. (S1) into (S2) and (S3), and assuming $|\dot{\theta}_i| \ll \Omega$, allows the power balance equation at each node to be written in the compact form

$$\frac{\mathrm{d}^2\theta_i}{\mathrm{d}t^2} + \gamma_i \frac{\mathrm{d}\theta_i}{\mathrm{d}t} = P_i - \sum_{j=1}^{n} K_{ij} \sin\left(\theta_i - \theta_j\right). \tag{S5}$$

This is the standard form of the swing equation, where the parameter γ_i is a damping term

$$\gamma_i = \frac{2D_i}{J_i} \tag{S6}$$

with units of s^{-1}. The coupling term is

$$K_{ij} = \frac{V_0^2 B_{ij}}{J_i \Omega} \tag{S7}$$

and has units of s^{-2}. If node i is not adjacent to node j, then $K_{ij} = 0$. The power term P_i also has units of s^{-2} and is given by

$$P_i = \frac{P_i^{\text{mech}} - D_i\Omega^2}{J_i\Omega}. \tag{S8}$$

P_i will be positive if i is a net generator, and negative if it is a net consumer. We assume for simplicity that the coupling, inertial, and damping terms are constant across the network so that $\gamma_i = \gamma \quad \forall i$. This allows Eq. (S5) to be written as

$$\frac{\mathrm{d}^2\theta_i}{\mathrm{d}t^2} + \gamma\frac{\mathrm{d}\theta_i}{\mathrm{d}t} = P_i - \kappa\sum_{j=1}^{n} A_{ij}\sin\left(\theta_i - \theta_j\right), \tag{S9}$$

where A is the adjacency matrix of the power network and κ is the network's coupling capacity:

$$\kappa = \frac{V_0^2 B}{J\Omega}. \tag{S10}$$

Eq. (S9) is the form of the swing equation employed throughout the main paper.

During normal operation, all machines are synchronised to the grid frequency Ω. This occurs when

$$P_i - \kappa\sum_{j=1}^{n} A_{ij}\sin\left(\theta_i - \theta_j\right) = 0 \tag{S11}$$

for all nodes i, which represents a steady state of Eq. (S5). Stable steady states are found by numerically integrating equation (S5).

During the operation of a power grid, some drift away from the reference frequency is tolerated. Any significant drift should be detected and trigger a shut-down to protect grid assets. For instance, the UK National Grid monitors grid frequency and rate of change of frequency (RoCoF), typically allowing RoCoF of 0.1 to 1 Hz/s (*41*). Following typical values used by the National Grid, we monitor the steady states of Eq. (S5) and remove any node i from the network if $\dot{\theta}_i > 1$ Hz or if the RoCoF $\ddot{\theta}_i > 1$ Hz/s.

Linear stability

The elementary example of a two-node network will now be used to demonstrate the fundamental dynamical properties of the swing equation. The network consists of a generator with power output P and a consumer with output $-P$. Let the generator and consumer be labelled nodes 1 and 2 respectively. The system is given by

$$\frac{\mathrm{d}^2\theta_1}{\mathrm{d}t^2} + \gamma\frac{\mathrm{d}\theta_1}{\mathrm{d}t} = P - \kappa\sin\left(\theta_1 - \theta_2\right) \tag{S12}$$

$$\frac{\mathrm{d}^2\theta_2}{\mathrm{d}t^2} + \gamma\frac{\mathrm{d}\theta_2}{\mathrm{d}t} = -P - \kappa\sin\left(\theta_2 - \theta_1\right) \tag{S13}$$

Subtracting Eq. (S13) from (S12) and defining the variable $\Delta\theta = \theta_1 - \theta_2$ allows the system to be written compactly as two first order ODEs:

$$\frac{\mathrm{d}}{\mathrm{d}t}(\Delta\theta) = \omega, \tag{S14}$$

$$\frac{\mathrm{d}\omega}{\mathrm{d}t} = 2P - \gamma\omega - 2\kappa\sin(\Delta\theta). \tag{S15}$$

There are two fixed points: $(\Delta\theta^*, \omega^*)_1 = (\arcsin(P/\kappa), 0)$ and $(\Delta\theta^*, \omega^*)_2 = (\pi - \arcsin(P/\kappa), 0)$. These two solutions are plotted as a function of P/κ in Fig. S1(A). They annihilate in a saddle node bifurcation at $\kappa_c = P$. The Jacobian evaluated at either of the two fixed points is

$$\mathbf{J} = \begin{pmatrix} 0 & 1 \\ x & -\gamma \end{pmatrix}, \tag{S16}$$

where $x = -2\sqrt{\kappa^2 - P^2}$ at $(\Delta\theta^*, \omega^*)_1$ and $x = 2\sqrt{\kappa^2 - P^2}$ at $(\Delta\theta^*, \omega^*)_2$. Both the trace and the determinant of the Jacobian are therefore negative at $(\Delta\theta^*, \omega^*)_2$ for all parameter values, indicating a saddle point. $(\Delta\theta^*, \omega^*)_1$ may be either a stable node, a stable degenerate node or a stable spiral depending on parameter choices. In particular, it will be a stable spiral for the range $0 < \gamma^2 < 8\sqrt{\kappa^2 - P^2}$, which typically encompasses the realistic lightly damped scenario of $\gamma < 1$. Both the saddle point and the stable spiral can be seen in the phase portrait in Fig. S1(B).

Note that the numerator of the coupling parameter, as defined in eq.(S10), is $V_0^2 B$. This is a quantity of power in units of Watts. By plugging in values of voltage and susceptance, this can be used to give the value of the critical coupling in Watts. Let us use $V_0 = 240$ V for the grid voltage. By the low resistance assumption, the susceptance is $B = 1/X_L$ where X_L is the inductive reactance. This is given by $X_L = 2\pi f L$ where $f = 50$ Hz is the grid frequency and L is the line inductance. Using a conservative estimate of $L = 10$ mH, the scaled coupling is $V_0^2 B = 18.3$ kW. This means the 2 node case above could handle a power of up to 18.3 kW before de-synchronisation. Lower inductances will give a higher kW limit.

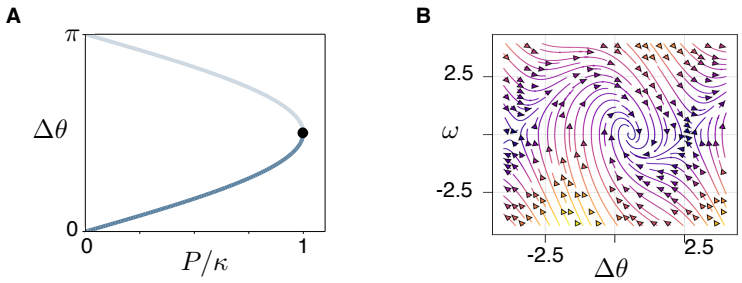

Figure S1: **Dynamics of the two-node system. A** Bifurcation diagram for the swing equation posed on a two-node network comprising one generator with output P and one consumer with output $-P$ linked by a single edge with coupling strength κ. $\Delta\theta$ is the phase difference of the two nodes. The stable fixed point at $\Delta\theta = \arcsin(P/\kappa)$ and the saddle point at $\Delta\theta = \pi - \arcsin(P/\kappa)$ annihilate at the critical coupling $\kappa_c = P$. **B** Phase portrait of the system, showing the spiral and saddle for parameter values $P = 0.5$, $\kappa = 1$ and $\gamma = 1$.

Cascade duration

This section provides further examples showing how cascade duration in seconds depends upon system parameters. Fig. S2 shows cascade durations as a function of normalised edge capacity α/α_* for various different system parameter values. Recall that α_* is the maximum flow volume in the network. The figure demonstrates that across the range of realistic parameter values of κ and γ, and across a range of network sizes n and randomness q, the durations follow a similar profile with respect to α/α_*. For low values of edge capacity, where cascades are typically catastrophic, the cascades have a very short duration. This duration increases as α, and hence survivability, increases. The durations peak at the critical value α_c/α_*. This peak value typically sits in the 20s to 30s range, although it can be much higher in the very low damping γ and low coupling κ regimes as well as in the case of networks being completely regular lattices ($q = 0$).

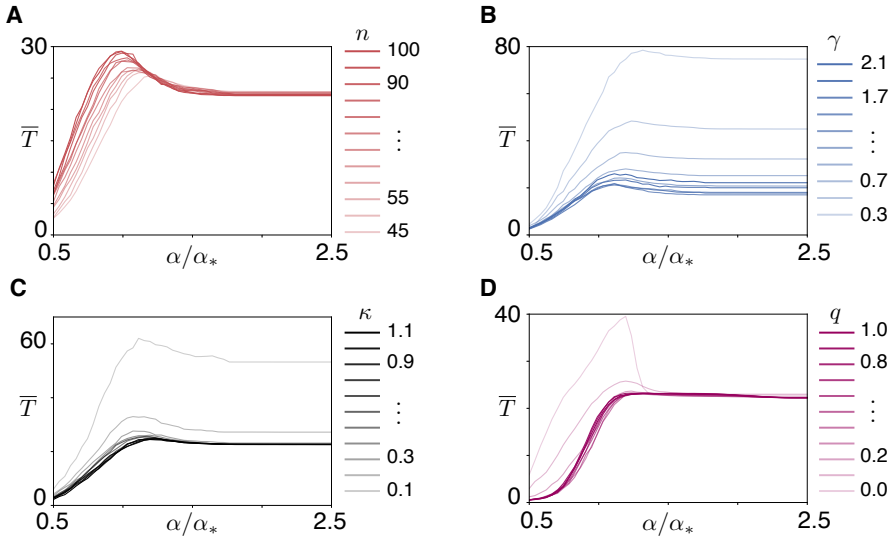

Figure S2: **Cascade duration as a function of normalised edge capacity.** Each line in each plot shows the mean cascade duration $\overline{T}$ in seconds as a function of normalised edge capacity α/α_* for ensembles of 500 networks. Error bars are omitted for visual clarity. In all cases, 20% of nodes are generators and 80% are consumers. **A** shows durations for a range of network sizes n, where $\gamma = \kappa = 1$ and $q = 0.1$. **B** shows durations for a range of damping γ, where $n = 50$ and $q = 0.1$. **C** shows durations for a range of coupling κ, where $n = 50$ and $\gamma = 1$. **D** shows durations for increasing topological randomness q, where $n = 50$ and $\kappa = \gamma = 1$.

Fig. S2 demonstrates that short durations are associated with small values of edge capacity α, and hence low cascade survivability. Longer durations are associated with less damaging cascades, which occur at higher values of α. This can can be seen more clearly by plotting individual values of $\mathcal{S}$ against T, for specific values of α. Such scatter plots are shown in Fig. S3. Each of the four panels shows $\mathcal{S}$ plotted against T for four different values of α in the

same ensemble of 500 networks with $q = 0.1$. In all cases, 20% of nodes are generators and 80% are consumers. Fig. S3A shows $\mathcal{S}$ versus T for $\alpha/\alpha_* = 0.75$, which is beneath the critical value α_c and corresponds to a situation where most cascades result in a low value of mean surviving edges $\overline{\mathcal{S}}$ and mean duration $\overline{T}$. This is confirmed in Fig. S3A, which shows most of the cascades are tightly clustered in the bottom-left of the plot. These cascades completely destroy the networks, giving values of $\mathcal{S} \approx 0$ and very short durations T . However, it is also clear that there is another cluster of less severe cascades, whose durations are longer. The result is that the durations are in fact bi-modal, as shown by the adjoining histogram in Fig. S3A. This same trend is also clear in Fig. S3B, which shows the case for $\alpha/\alpha_* = 1$. This is still beneath the critical value. The second cluster has now grown and encompasses most of the cascades. Panel S3C shows the situation at the critical point α_c/α_*. Here, a third cluster has emerged at the top centre-left which now contains the vast majority of the cases. This can be seen as the very small, bright yellow blob. These are the cascades which cause little damage, and whose durations are roughly the same as the second cluster of intermediately damaging cascades. For α greater than α_c, as shown in Fig. S3D, the only cluster of any significance remaining is that of the cascades causing little damage, which emerged in panel C. In summary, a short duration is associated with catastrophic cascades, while cascades that cause little impact have a longer and approximately constant duration.

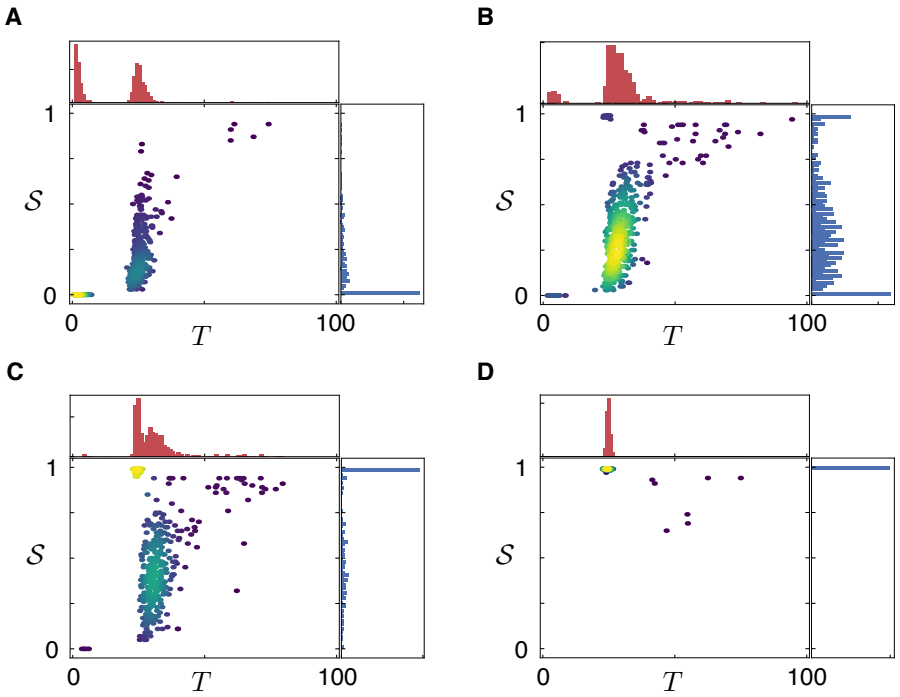

Figure S3: **Fraction of edges surviving cascades against cascade duration.** Each panel is a scatter plot of the duration T of a cascade against the fraction $\mathcal{S}$ of surviving edges, for an ensemble of 500 random networks with configuration, where 20% of nodes are generators and remainder are consumers. Each panel has a different value of edge capacity α. The values of α for panels **A** to **D** are, respectively, 0.75, 1, 1.21, and 2. The colours of the scatter points encode the density of points; the brighter the denser. Adjoining each axis are histograms giving a picture of the distribution of each variable

Cascade resilience

This section presents further results of cascade resilience ρ as a function of node type composition. Figure S4 shows results for networks with $n = 100$ and common degree $k = 4$ for four different values of q. As q increases, the regions of high ρ, indicating low resilience, broaden from the edges. However, in all cases, the most resilient configuration, indicated by low ρ, are located in the bottom-centre of the simplex and correspond to networks with commensurate numbers of consumers and generators and few passive nodes. Figure S5 shows the case for smaller networks with $n = 50$ nodes. The trends in resilience with respect to consumer-generator proportions are the same as those for larger networks, although the values of ρ are slightly reduced.

Figure S4: **Resilience as a function of consumer-generator numbers for networks with 100 nodes.** Panels **A** to **D** show $\overline{\rho}$ projected onto the node configuration simplex for Watts-Strogatz networks with topological randomness parameter $q = 0$, 0.2, 0.4 and 1, respectively. Simplexes **A** to **D** therefore represent increasing structural randomness from regular lattices to Poisson networks. All networks have $n = 100$ and common degree $K = 4$. Each pixel shows $\overline{\rho}$ obtained from an ensemble average over 100 network realisations where source and sink locations are allocated randomly. $\overline{\rho}$ is computed using the algorithm outlined in the main paper.

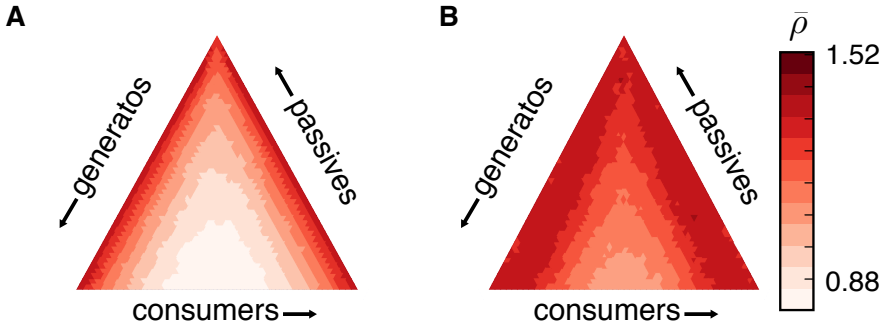

Figure S5: **Resilience as a function of consumer-generator numbers for networks with 50 nodes.** **A** and **B** show $\overline{\rho}$ projected onto the node configuration simplex for Watts-Strogatz networks with topological randomness parameter $q = 0$ and $q = 0.2$, respectively. All networks have $n = 100$ and common degree $K = 4$. Each pixel shows $\overline{\rho}$ obtained from an ensemble average over 100 network realisations where source and sink locations are allocated randomly.

Seasonal and diurnal variation in micro-grid dynamics

UK household power consumption and PV generation data (*28, 29*) are used to construct models of micro-grids. Their dynamics can be simulated for different seasons of the year and for different levels of photovoltaic (PV) uptake. Using a projection method, the numbers of generators and consumers operating concurrently at a given point in time on the grid can be converted into a point on a triangular phase-plane, or simplex. In particular, the micro-grids are modelled as networks whose n nodes are households with power demand and output specified by the data. The power output $P_i(t)$ in kW of a node i at time t is $g_i(t) - c_i(t)$, where $g_i(t)$ and $c_i(t)$ are the node's generation and output, respectively. The network then has a power vector $\mathbf{P} \in \mathbb{R}^n$, with components corresponding to the power outputs of the nodes. From this, three dimensionless consumer-generator coordinates are computed as follows. The generator density is defined as

$$\eta_+ := \frac{1}{n \max(\mathbf{P})} \sum_{x \in \mathbf{P}^+} x, \tag{S17}$$

where $\mathbf{P}^+$ is the vector containing only the positive elements of $\mathbf{P}$. Consumer density is likewise defined as

$$\eta_- := \frac{1}{n \min(\mathbf{P})} \sum_{x \in \mathbf{P}^-} x, \tag{S18}$$

where $\mathbf{P}^-$ contains the negative components of $\mathbf{P}$. Finally, the passivity of the network is

$$\eta_p := 1 - \eta_+ - \eta_-. \tag{S19}$$

These three numbers (η_+, η_-, η_p) allow a micro-grid's composition of net consumers and generators to be represented as a point on the triangular simplex, as demonstrated in Fig. S6. For instance, if the micro-grid is dominated by consumers, with only one node acting as a generator, then it will be located on the right hand edge of the simplex. If the micro-grid instead has an equal number of effective consumers and generators, then it will be located along the vertical centre line of the simplex. As time progresses in the micro-grid and the numbers of effective consumers and generators change, the grid will sweep a trajectory through the simplex. Examples of such trajectories, captured over the course of a week, are shown in Fig. S6. Each simplex in the Figure shows trajectories for 50 different realisations of a micro-grid with $n = 50$ nodes, where the time-series for each node has been drawn uniformly at random. Each of the trajectories within the ensembles can be seen in pale red, while the ensemble mean is indicated by the thick red line. The different simplexes in Fig. S6 each show cases for different seasons of the year and different levels of household PV uptake. The Figure demonstrates that, on average, the micro-grid trajectories travel further and spend longer on the left-hand side of the simplex as the level of PV uptake increases and as the seasons tend towards summer.

The robustness properties of the micro-grids are characterised by the critical coupling κ_c required for synchronous operation, and the critical edge capacity α_c required to survive a cascading failure. These quantities vary as the proportions of consumers and generators in the grids

change. Thus, the diurnal trajectories of the grids through the simplex result in daily variations in robustness. To gauge these variations in robustness, the quantities κ_c and $\rho = \alpha_c/\alpha_*$, where α_* is the minimum edge capacity required for a network to function normally, are computed for networks of fixed size n with varying numbers of generators and consumers. These computations utilise the reduced dimensional model of power grid dynamics given in Eq. S5. This allows the construction of simplexes containing values of κ_c and ρ for all possible consumer-generator compositions of a network with fixed size. The quantities κ_c and ρ are dimensionless. To evaluate the robustness of the fully dimensional models, whose node powers profiles are in kW, their (η_+, η_-, η_p) locations on the simplex computed from Eqs. (S17-S19) are scaled up by a factor of n to give their locations on the ρ and κ_c simplexes from which (κ_c, ρ) are sampled.

Fig. S7 shows the variation in κ_c over the course of a week for an ensemble of micro-grids with $q = 0$ and 100% PV uptake in both the summer and the winter. Recall that low values of κ_c effectively mean the grid can synchronise more readily. The lowest values of κ_c are in the centres of the simplexes, corresponding to points in time where there are roughly equal numbers of consumers and generators operating concurrently. The Figure shows that in the winter there are daily dips in κ_c as the micro-grids move into the robust central region of the space. In the summer however, these daily dips are reduced to brief twice-daily spikes, since the grids spend much less time in the centre. This is due to the increased PV production causing grids to spend midday dominated by production. Figure S8 shows equivalent results for random networks with $q = 1$. The same daily trends occur here as in the $q = 0$ case, although the κ_c values are in general lower, reflecting the higher synchronisability of more random networks.

Figures S9 and S10 show the locations of randomly triggered cascading failures occurring in micro-grids with different levels of PV uptake and at different times of the year. The Figures show that in the winter, the values of α_c required to survive a cascade are typically low and are associated with failures occurring higher up in the simplex, where the grids are dominated by mostly passive nodes. In the summer, for high PV uptake, the values of α_c are much larger. This is due to the increased PV activity driving the grids further down the simplex as they become dominated by generation. Figure S11 shows that these results broadly hold for the case of more random networks with $q = 1$.

Figure S12 shows trajectories for ensembles of micro-grids at various levels of PV uptake during the winter and the summer, where each house is equipped with a battery. The figure demonstrates that batteries, in all cases, are unable to manipulate trajectories into the resilient bottom-centre region of the simplex.

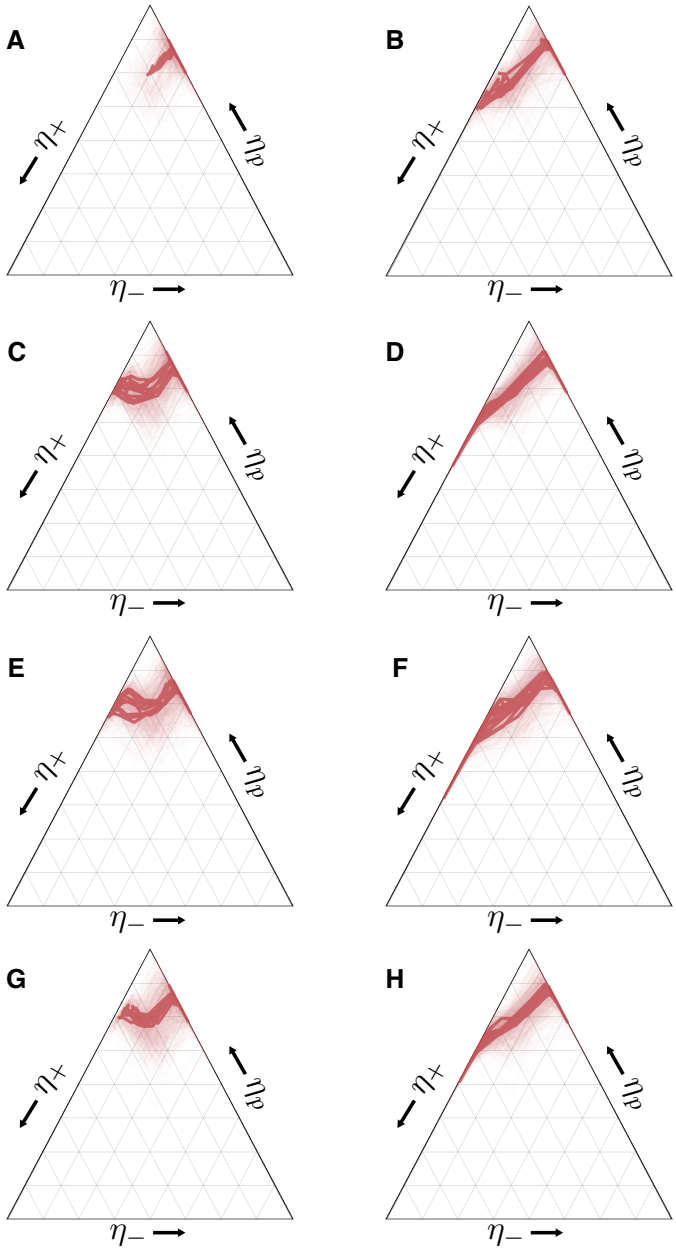

Figure S6: **Weekly micro-grid trajectories.** Each panel shows trajectories through the consumer-generator simplex space for ensembles of 50 micro-grids each with $n = 50$ houses over the course of a week. The quantities η_+, η_-, $\eta_p \in [0, 1]$ are the consumer, generator and passive node densities, respectively. Light red lines are the trajectories of individual ensemble members, and the this red line is the ensemble mean trajectory. The left column of simplexes – **A**, **C**, **E** and **F** – are for the case of 50% PV uptake in the winter, spring, summer, and autumn respectively. The right hand column shows the corresponding case for 100% PV uptake.

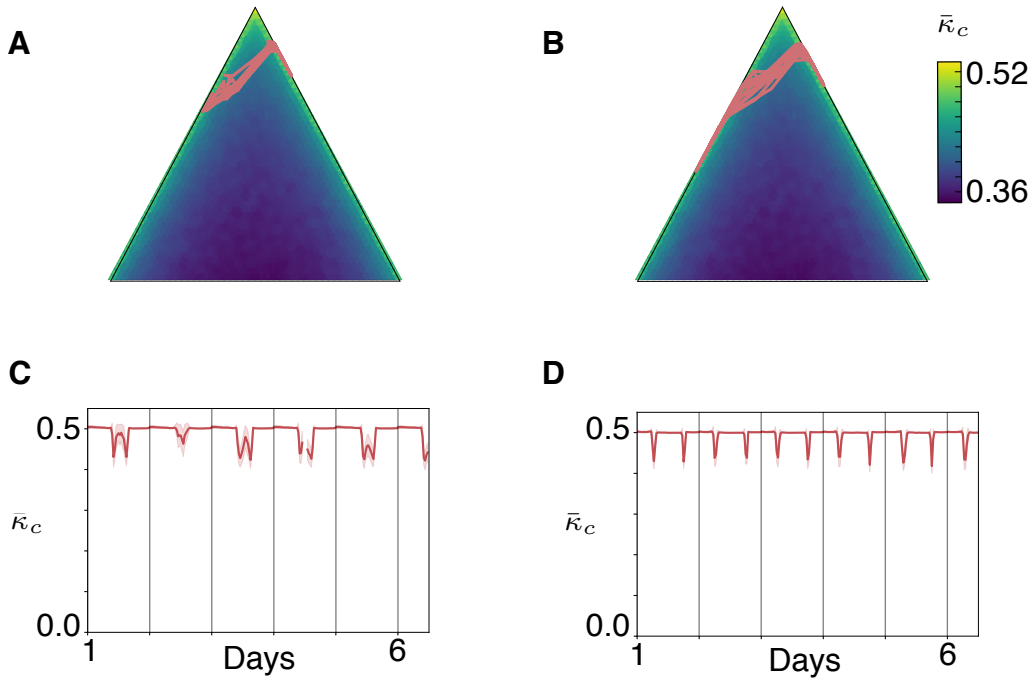

Figure S7: **Variations in critical coupling for regular lattices.** **A** and **B** show the ensemble average trajectory through the critical coupling κ_c simplex for micro-grids with $n = 50$ houses in the winter and summer respectively with 100% PV uptake. The grids here are assumed to have a lattice like structure. **C** and **D** show the corresponding weekly variation in κ_c in winter and summer respectively.

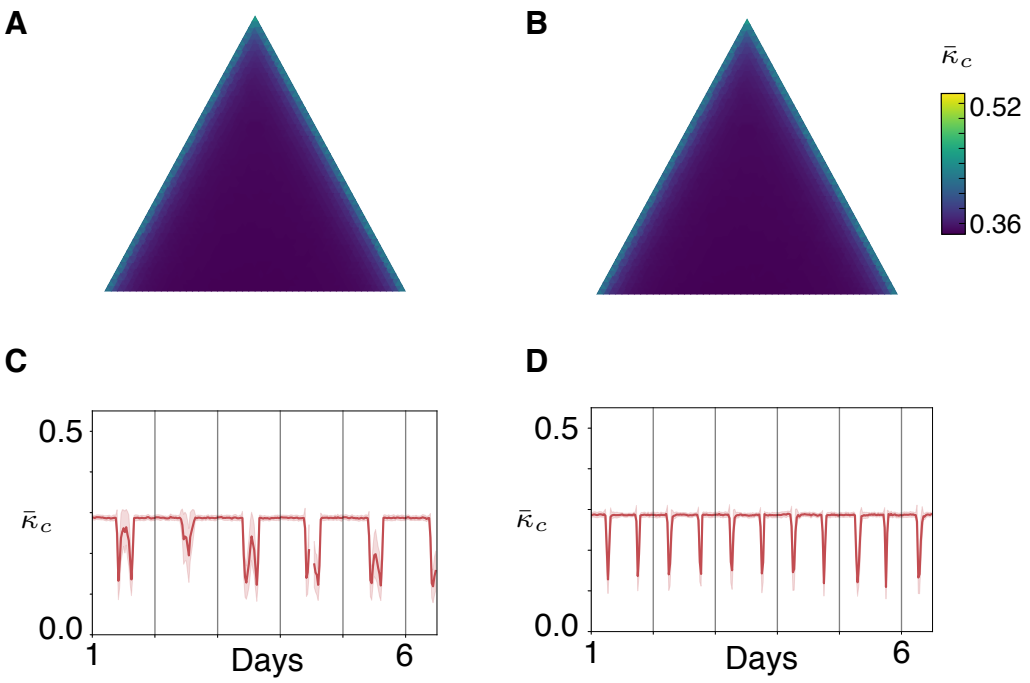

Figure S8: **Variations in critical coupling for Poisson networks. A** and **B** show the ensemble average trajectory through the critical coupling κ_c simplex for micro-grids with $n = 50$ houses in the winter and summer respectively with 100% PV uptake, with $q = 1$. **C** and **D** show the corresponding weekly variation in κ_c in winter and summer respectively.

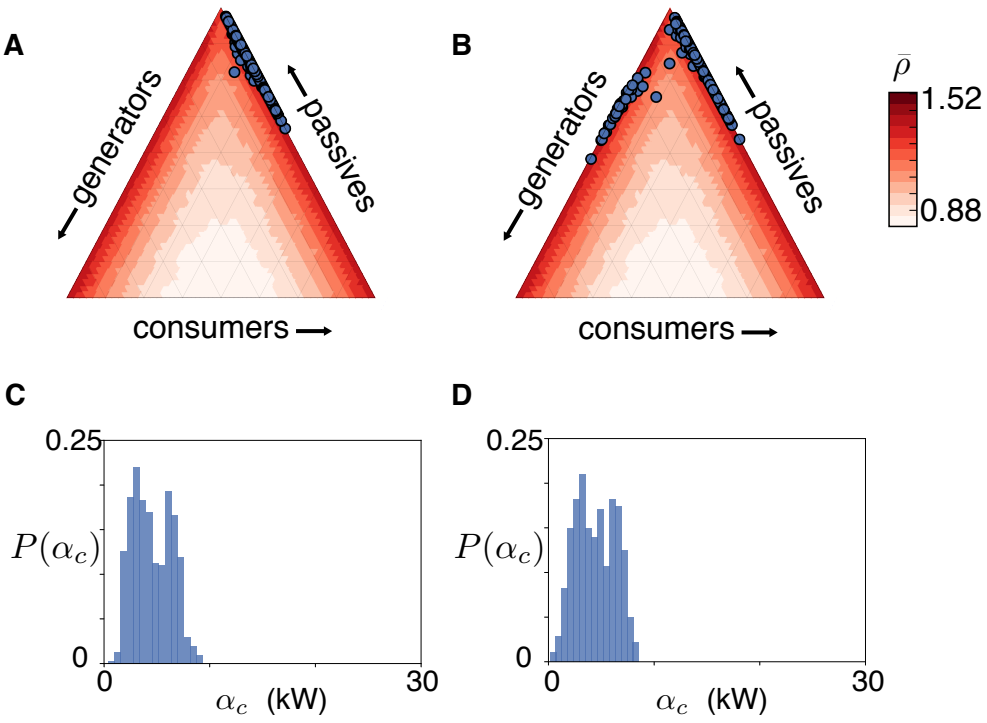

Figure S9: **Impact of PV uptake on resilience during winter.** **A** and **B** show the locations of randomly triggered cascading failures occurring during the winter for micro-grids with 50% and 100% PV uptake respectively. $\overline{\rho}$ is the resilience measure giving the amount of capacity α_c required to survive a cascade relative to the capacity required for normal operation. Histograms **C** and **D** show the corresponding values of α_c for the 50% and 100% cases.

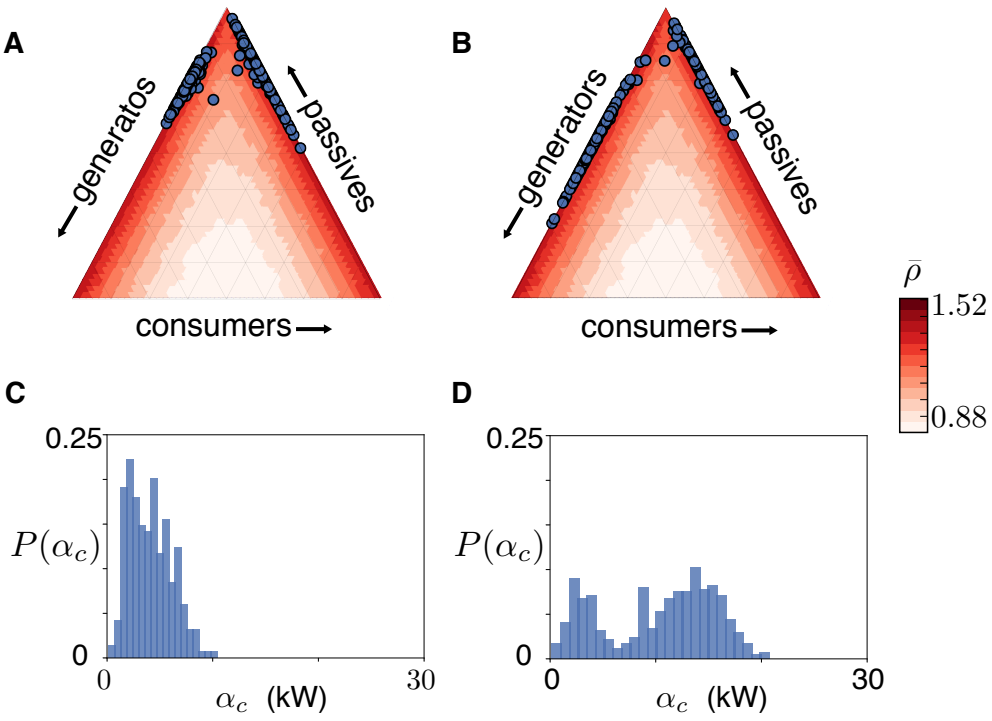

Figure S10: **Impact of PV uptake on resilience during summer. A** and **B** show the locations of randomly triggered cascading failures occurring during the summer for micro-grids with 50% and 100% PV uptake respectively. $\overline{\rho}$ is the resilience measure giving the amount of capacity α_c required to survive a cascade relative to the capacity required for normal operation. Histograms **C** and **D** show the corresponding values of α_c for the 50% and 100% cases.

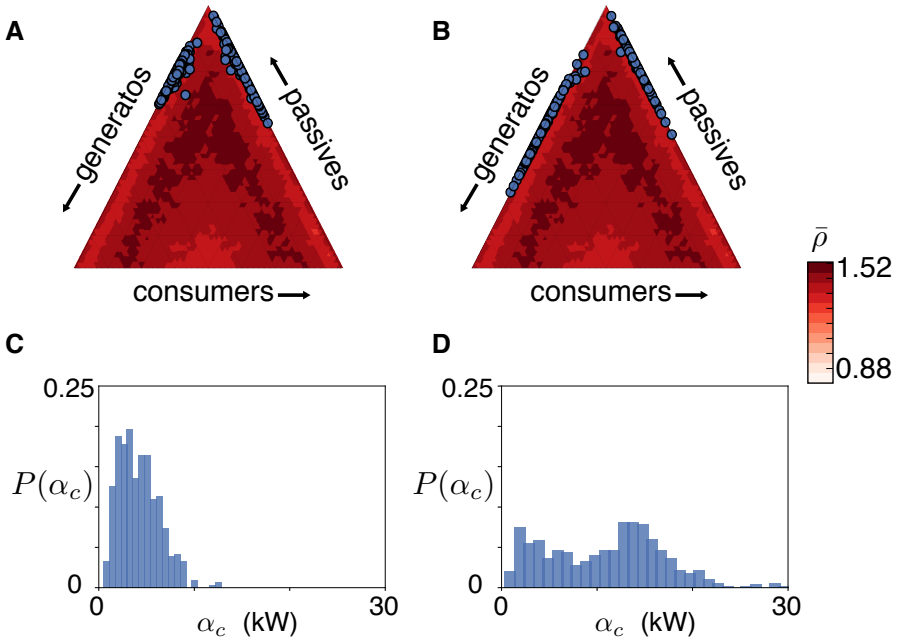

Figure S11: **Impact of PV uptake on resilience during summer for highly random networks. A** and **B** show the locations of randomly triggered cascading failures occurring during the summer for micro-grids with 50% and 100% PV uptake respectively. In both cases, $q = 1$ for all networks. $\overline{\rho}$ is the resilience measure giving the amount of capacity α_c required to survive a cascade relative to the capacity required for normal operation. Histograms **C** and **D** show the corresponding values of α_c for the 50% and 100% cases.

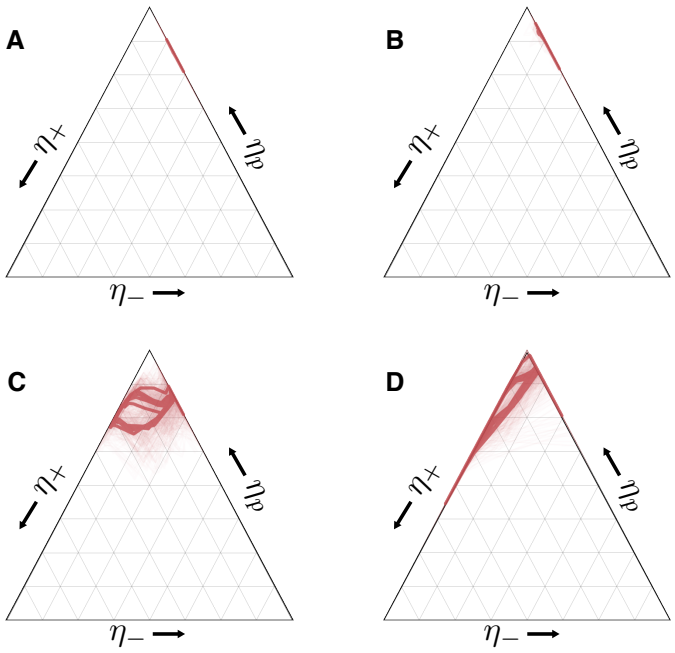

Figure S12: **Weekly trajectories through the node configuration simplex for battery equipped micro-grids.** All networks have $n = 50$ nodes. Each panel shows the weekly mean trajectory of an ensemble of 50 micro-grids where every house with PV is equipped with a battery. Panels **A** and **B** show the case for 50% and 100% PV uptake, respectively, in the winter. Panels **C** and **D** show the case for 50% and 100% PV uptake, respectively, in the summer.

REFERENCES AND NOTES

1. UK Department for Business, Energy and Industrial Strategy, “Energy Trends: U.K. Renewables” (2020); www.gov.uk/government/statistics/energy-trends-section-6-renewables [accessed 16 February 2021].

2. UK Government, “The Climate Change Act 2008” (UK Statutory Instrument 2019/1056, 2008); www.legislation.gov.uk/uksi/2019/1056/contents/made.

3. United Nations, “The Paris Agreement” (2015); https://unfccc.int/process-and-meetings/the-paris-agreement/the-paris-agreement [accessed 16 February 2021].

4. I. Dobson, B. A. Carreras, V. E. Lynch, D. E. Newman, Complex systems analysis of series of blackouts: Cascading failure, critical points, and self-organization. *Chaos* **17**, 026103 (2007).

5. D. J. Watts, A simple model of global cascades on random networks. *Proc. Natl. Acad. Sci. U.S.A.* **99**, 5766–5771 (2002).

6. B. A. Carreras, V. E. Lynch, I. Dobson, D. E. Newman, Critical points and transitions in an electric power transmission model for cascading failure blackouts. *Chaos* **12**, 985–994 (2002).

7. A. Motter, Y.-C. Lai, Cascade-based attacks on complex networks. *Phys. Rev. E* **66**, 065102 (2003).

8. P. Crucitti, V. Latora, M. Marchiori, Model for cascading failures in complex networks. *Phys. Rev. E* **69**, 045104 (2004).

9. Y. Yang, T. Nishikawa, A. E. Motter, Small vulnerable sets determine large network cascades in power grids. *Science* **358**, eaan3184 (2017).

10. S. Pahwa, C. Scoglio, A. Scala, Abruptness of cascade failures in power grids. *Sci. Rep.* **4**, 3694 (2014).

11. D. Witthaut, M. Timme, Nonlocal effects and countermeasures in cascading failures. *Phys. Rev. E* **92**, 032809 (2015).

12. C. D. Brummitt, R. M. D'Souza, E. A. Leicht, Suppressing cascades of load in interdependent networks. *Proc. Natl. Acad. Sci. U.S.A.* **109**, E680–E689 (2012).

13. A. Scala, P. G. De Sanctis Lucentini, G. Caldarelli, G. D'Agostino, Cascades in interdependent flow networks. *Physica D* **323-324**, 35–39 (2016).

14. A. Fouad, V. Vittal, *Power System Transient Stability Analysis Using the Transient Energy Function Method* (Pearson Education, 1991).

15. T. Nishikawa, A. E. Motter. Comparative analysis of existing models for power-grid synchronization. *New J. Phys.* **17**, 015012 (2015).

16. A. E. Motter, S. A. Myers, M. Anghel, T. Nishikawa. Spontaneous synchrony in power-grid networks. *Nat. Phys.* **9**, 191–197 (2013).

17. B. Schäfer, D. Witthaut, M. Timme, V. Latora. Dynamically induced cascading failures in power grids. *Nat. Commun.* **9**, 1975 (2018).

18. Y. Yang, A. E. Motter. Cascading failures as continuous phase-space transitions. *Phys. Rev. Lett.* **119**, 248302 (2017).

19. D. Witthaut, M. Timme. Braess's paradox in oscillator networks, desynchronization and power outage. *New J. Phys.* **14**, 083036 (2012).

20. S. Parhizi, H. Lotfi, A. Khodaei, S. Bahramirad. State of the art in research on microgrids: A review. *IEEE Access* **3**, 890–925 (2015).

21. A. Halu, A. Scala, A. Khiyami, M. C. González. Data-driven modeling of solar-powered urban microgrids. *Sci. Adv.* **2**, e1500700 (2016).

22. B. Schäfer, C. Grabow, S. Auer, J. Kurths, D. Witthaut, M. Timme. Taming instabilities in power grid networks by decentralized control. *Eur. Phys. J. Spec. Top.* **225**, 569–582 (2016).

23. M. Rohden, A. Sorge, M. Timme, D. Witthaut. Self-organized synchronization in decentralized power grids. *Phys. Rev. Lett.* **109**, 064101 (2012).

24. O. Smith, J. Crowe, R. D. O'Dea, K. I. Hopcraft. The price of anarchy in flow networks as a function of node properties. *Europhys. Lett.* **127**, 18001 (2019).

25. O. Smith, J. Crowe, E. Farcot, R. D. O'Dea, K. I. Hopcraft. Cascading failures in networks of heterogeneous node behavior. *Phys. Rev. E* **101**, 020301 (2020).

26. W. Quattrociocchi, G. Caldarelli, A. Scala. Self-healing networks: Redundancy and structure. *PLOS ONE* **9**, e87986 (2014).

27. F. Morone, L. Ma, H. Makse, A. Scala, Enhancing network resilience via self-healing, in *2016 IEEE Workshop on Environmental, Energy, and Structural Monitoring Systems* (IEEE, 2016), pp. 1–5.

28. G. Filatrella, A. H. Nielsen, N. F. Pedersen, Analysis of a power grid using a Kuramoto-like model. *Eur. Phys. J. B* **61**, 485–491 (2008).

29. D. Manik, D. Witthaut, B. Schäfer, M. Matthiae, A. Sorge, M. Rohden, E. Katifori, M. Timme. Supply networks: Instabilities without overload. *Eur. Phys. J. Spec. Top.* **223**, 2527–2547 (2014).

30. D. J. Watts, S. H. Strogatz, Collective dynamics of 'small-world' networks. *Nature* **393**, 440–442 (1998).

31. UK Power Networks, SmartMeter Energy Consumption Data in London Households (2014); https://data.london.gov.uk/dataset/smartmeter-energy-use-data-in-london-households [accessed on 20 January 2019].

32. UK Power Networks, Photovoltaic (PV) Solar Panel Energy Generation Data (2014); https://data.london.gov.uk/dataset/photovoltaic--pv--solar-panel-energy-generation-data [accessed on 21 January 2019].

33. Institution of Engineering and Technology, *Requirements for Electrical Installations, IET Wiring Regulations, Eighteenth Edition, British Standard 7671:2018* (Institution of Engineering and Technology, 2018).

34. Tesla, Tesla Powerwall 2 Datasheet (2018); www.tesla.com/sites/default/files/pdfs/powerwall/Powerwall%202_AC_Datasheet_en_GB.pdf [accessed on 10 October 2020].

35. S. Korjani, A. Facchini, M. Mureddu, A. Rubino, A. Damiano, Battery management for energy communities—Economic evaluation of an artificial intelligence-led system. *J. Clean. Prod.* **314**, 128017 (2021).

36. W. Kempton, J. TomiÄ, Vehicle-to-grid power fundamentals: Calculating capacity and net revenue. *J. Power Sources* **144**, 268–279 (2005).

37. M. Mureddu, A. Facchini, A. Scala, G. Caldarelli, A. Damiano. A complex network approach for the estimation of the energy demand of electric mobility. *Sci. Rep.* **8**, 268 (2018).

38. M. Musio, A. Damiano, Analysis of vehicle to grid and energy storage integration in a virtual power plant, in *IECON 2014 - 40th Annual Conference of the IEEE Industrial Electronics Society* (IEEE, 2014), pp. 3094–3100.

39. J. Zhao, D. Li, H. Sanhedrai, R. Cohen, S. Havlin. Spatio-temporal propagation of cascading overload failures in spatially embedded networks. *Nat. Commun.* **7**, 10094 (2016).

40. Y. Kornbluth, G. Cwilich, S. V. Buldyrev, S. Soltan, G. Zussman. Distribution of blackouts in the power grid and the Motter and Lai model. *Phys. Rev. E* **103**, 032309 (2021).

41. A. Dyśko, D. Tzelepis, C. Booth, *Assessment of Risks Resulting from the Adjustment of Vector Shift (VS) Based Loss of Mains Protection Settings* (Institute for Energy and Environment, 2017); www.nationalgrid.com/sites/default/files/documents/Appendix%202%20Strathclyde%20Report%202.pdf.

42. O. Smith, o-smith/GridResilience: Paper version of code (v1.0.0). Zenodo (2021); https://doi.org/10.5281/zenodo.5702877.

43. Y. Chen, R. Hesse, D. Turschner, H. Beck, Improving the grid power quality using virtual synchronous machines, in *2011 IEEE International Conference on Power Engineering, Energy and Electrical Drives* (IEEE, 2011), pp. 1–6.